Int. J. Multiphase Flow Vol. 8, No. 5, pp. 475–490, 1982
Printed in Great Britain.

0301-9322/82/050475-16$03.00/0
Pergamon/Elsevier

EXPERIMENTAL STUDY OF VORTEX EMISSION BEHIND BLUFF OBSTACLES IN A GAS LIQUID VERTICAL TWO-PHASE FLOW

J-P. HULIN, C. FIERFORT and R. COUDOL

Physics Engineering Department, Etudes & Productions Schlumberger, 26 rue de la Cavée, 92140 Clamart, France

(*Received* 15 *December* 1980; *in revised form* 18 *December* 1981)

Abstract—Vortex emission behind cylinders with trapezoidal cross section was experimentally studied in air–water vertical two-phase flows (liquid velocities vary from 45 cm/s to 2 m/s inside a 15 cm ID pipe); the void fraction ranged from 0 to 25%. The measurements were performed at room pressure and temperature. Two flow regimes were observed. For void fraction smaller than 10% vortex emission remained stable and its frequency sharply defined. However, the rms amplitude of the associated pressure fluctuations strongly decreased. These results were explained by bubble trapping inside the vortex cores. This effect was verified experimentally and analyzed using optical fiber probe measurements. Above a 10% void fraction, vortex emission became erratic. Its spectrum became broader but could be identified up to 25% void fraction.

INTRODUCTION

Periodic emission of vortices behind bluff bodies submerged in a fluid flow is very frequently observed in a large variety of fluids and obstacles sizes (Strouhal 1878; Marris 1964; Mair & Maul 1971). A so-called von-Karman vortex street appears downflow, made up of two rows of vortices of opposite circulation. Understanding this phenomenon is important, either to avoid vortex-induced oscillations in many large structures (buildings, bridges, cooling towers) or to take advantage of them as in vortex flowmeters using sharp-edged obstacles; these devices are based on the nearly linear variation of the vortex emission frequency with fluid velocity (White *et al.* 1974, Medlock 1976).

Vortex emission and vortex flowmeters have been extensively studied in single phase liquid and gas flows. On the contrary, while two-phase flows are more and more frequently encountered in practical applications (Delhaye *et al.* 1981), for instance in nuclear, petroleum and chemical engineering, very few experimental data are available on vortex emission in such flows (for example, bubble trapping is observed inside vortices generated by hydraulic surges (Goldring *et al.* 1980, Auton 1981).

In addition, from a more fundamental point of view, it is quite interesting to determine whether the disorder associated with two-phase flows can destroy the orderly von Karman vortex street structure or whether some degree of order will be retained. Moreover, the percentage of each constituent of the flow is a parameter that may vary with time and position. One may very well imagine that vortex emission does not induce only velocity variations but that local fluctuations of the mixture composition may also occur.

We present here an experimental study of vortex emission in vertical air–water upward two-phase flows. The obstacle geometry is similar to that used in vortex flowmeters, and the flow regime is bubble flow or, sometimes, low void fraction slug flow.

We measured the frequency, amplitude and bandwidth of the vortex oscillations in a wide range of void fractions (0–25%) and liquid velocities (0–2 m/s) inside a 15 cm ID pipe.

We have, in addition, measured variations of the spatial period λ of the von Karman vortex street in the wake of the obstacle. For that purpose phase shift and coherence measurements (Bendat & Piersol 1980) were performed on a two-obstacle setup. These measurements gave information on the vortex street stability as the vortices were carried away from the obstacles.

1. EXPERIMENTAL PROCEDURE

1.1 *Vortex generating assembly*

Vortices were emitted by two cylinders of trapezoidal cross section located on two parallel diameters of a 15 cm ID vertical flow tube spaced 18 cm apart (figure 1). The obstacles were 23 mm thick with a 28° apex angle and have a width $W = 35$ mm (figure 2).

In this two-obstacle setup, vortex emission on the downflow obstacle was triggered by the vortices emitted by the first. This allowed us to gain, through phase shift and coherence measurements between the signals from the two obstacles, additional information on the downflow propagation of the vortex street. In case the vortex emission process had been

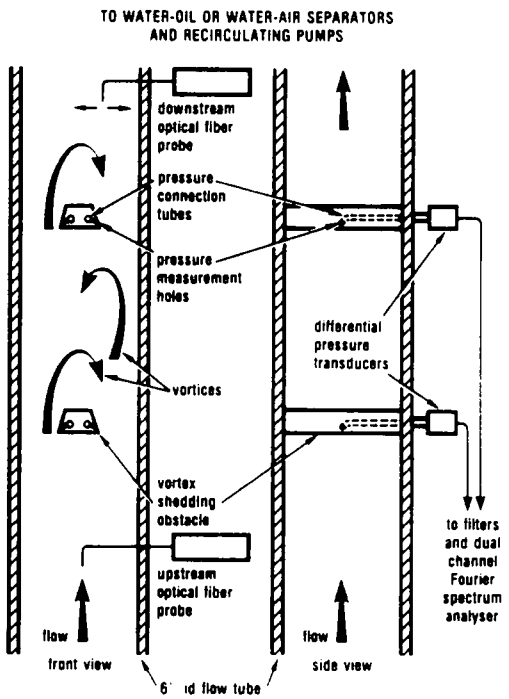

Figure 1. General view of experimental setup for vortex emission study in air–water diphasic vertical flows.

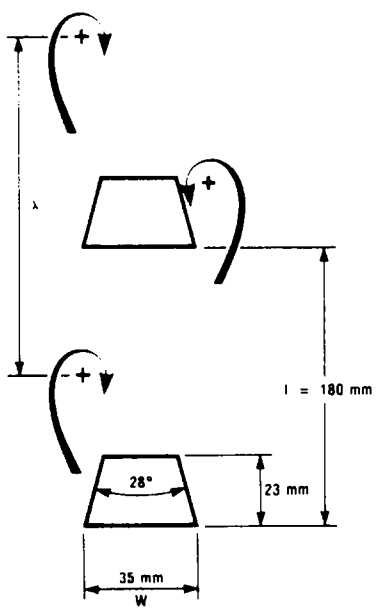

Figure 2. Cross section of vortex generating double-obstacle assembly.

distorted by this setup, we performed some cross-check measurements on a single obstacle. The variations of the vortex emission signal frequency, amplitude and bandwidth confirmed the other results and gave very similar frequency and amplitude values. We chose obstacles with sharp edges for vortex generation instead of circular cylinders (which have been much more extensively studied) for two reasons:

— Such obstacles are the only ones used for flow metering purposes because of the very constant vortex emission frequency/flow rate ratio they allow.

— The vortex emission process does not disappear for Reynolds numbers of the order of 10^4–10^5, as is the case for circular cylinders. This seems due to the boundary layer separation points being fixed at the front edges of the obstacle instead of moving, as is the case of a circular cylinder.

The width of the obstacles was about 0.23 times the pipe diameter creating a rather large obstruction across the flow. This width/pipe diameter ratio has been chosen because it provided very strong vortex emission signals and is close to the values encountered in most practical applications.

1.2 *Vortex emission detection*

Vortex emission was detected by monitoring oscillations of the pressure difference across the obstacle: these were induced by the alternate emission of vortices on each side. The power spectra of each individual signal, the phase shift and coherence spectra between them were then computed by an HP 5451C dual-channel spectrum analyzer. The vortex emission frequency was determined with a precision of ±0.3% at low void fractions. The relative precision of the pressure fluctuation amplitude measurements was ±2% under the same conditions. When the coherence between signals from the two obstacles was above ±0.9, the phase shift could be measured with an absolute precision of ±3°.

1.3 *Two-phase flow generation and measurement*

Water flow rates varied between 0 and 120 m^3/h and were measured by turbine flowmeters to ±0.5%. Gas flow rates ranged from 0 to 70 m^3/h (STP), and were measured by orifice flowmeters (precision 3%).

The void fraction in the center of the flow tube was measured by an optical fiber probe.† This probe was located 30 cm upstream of the obstacles to avoid void fraction variations induced by them. It detected the phase (liquid or gas) surrounding a 100 μm dia. tip. In some cases we have used its output directly, otherwise, an electronic circuit computed the percentage of the total measurement time spent in air (Danel & Delhaye 1971, Jones & Delhaye 1976); the void fraction profile can be determined by moving the probe along a diameter, but this measurement was too lengthy to be performed for all sets of gas and liquid flow-rate values.

Another possible parameter-characterizing the flow is the quality. It is not equal to the area void fraction because of the effect of the relative velocity between liquid and gas. We found that correlating the data with the quality was physically less meaningful than when we used the void fraction.

All measurements were performed near the top of a 12 m high vertical flow tube in order to obtain a reasonably stable fully developed flow. Air was injected axially at the bottom through a 16 mm ID tube. The typical bubble size was 2–4 mm. The temperature variations were kept small (typically a few °C around 25°C).

2. SINGLE-PHASE FLOW MEASUREMENTS

These measurements provide a basis for comparison with two-phase flow experiments and tested the validity of our two-obstacle coherence and phase shift measurements.

†Type 7401 optical fiber probe. Manufacturer: AID (ZIRST, Chemin des Clos, 38240 Meylan, France).

We measured the vortex emission frequency at average liquid velocities $\bar{V}_L$ varying between 0.3 and 1.5 m/s.

$\bar{V}_L$ is defined by:

$$\bar{V}_L = \frac{Q_L}{A}. \quad [1]$$

Where Q_L is the water flow rate and A the tube cross section. The Strouhal number S defined as $S = W\nu/\bar{V}_L$ is constant in that range and equal to 0.22 ± 0.01. Here W is the diameter of the obstacle and ν is the frequency of the vortices.

Following Goldstein (1950), we assume that the vortex street structure is carried downflow at a velocity $V_V = 0.92\bar{V}_L$, and the wavelength or the distance between two consecutive vortices on one row (figure 2) is

$$\lambda = \frac{V_v}{\nu} = 0.92\frac{\bar{V}_L}{\nu} = 14.6\,\text{cm}. \quad [2]$$

Hence, $\bar{V}_L/\nu = \text{const}$ means that the vortex street wavelength λ is constant and depends only on the obstacle size and geometry. (However, in this estimation of λ, we have not taken into account possible variations of either $\bar{V}_L$ or λ due to the presence of the two obstacles.)

Another value for λ can be estimated from measurements of the phase shift $\Delta\varphi$ between vortex-generated pressure oscillations by using the relation:

$$\Delta\varphi = 2\pi\frac{l}{\lambda} \quad [3]$$

where l is the spacing between obstacles (figure 2). $\Delta\varphi$ is measured practically as the phase of the complex cross spectrum between signals from the two obstacles.

Experimentally, $\Delta\varphi = 444 \pm 3°$ in the range of $\bar{V}_L$ values explored whence $\lambda = 14.6$ cm for $l = 18$ cm. This surprisingly good agreement, in view of the crude approximations involved, indicates only that both procedures of evaluation for λ are physically correct.

The rms amplitude of the pressure oscillations has also been measured: it is proportional to Q_L^2. Some lower velocity (0–40 m^3/h) measurements with kerosene of density $\rho = 750$ kg/m^3 verified that the amplitude is also roughly proportional to ρ.

3. AIR–WATER TWO-PHASE FLOW MEASUREMENTS

3.1 *General features of experimental results*

We analyzed pressure oscillations from both obstacles at water superficial velocities between 0.3 and 1.7 m/s and void fractions α_G measured upstream of the obstacle on the axis of the flow tube between 0 and 25% (lower velocities in two-phase flows and higher void fractions yielded poor vortex-induced oscillation spectra).

Two different regimes can be identified after a first examination of the direct signals and their power spectra. For α_G below about 10% (figure 3), vortex-induced oscillations remain permanent; their amplitude is rather constant with time. Although the mean value of the amplitude decreases, the power spectra display very sharp peaks.

For higher α_G's vortex oscillations become erratic, their amplitude fluctuates a great deal and the power spectra display much broader peaks (figure 3).

3.2 *Variation of the vortex emission frequency with void fraction*

Key information on the behavior of vortex emission in two-phase flows is provided by the variations of its frequency with the amount of air injected. For single phase flows, the Strouhal

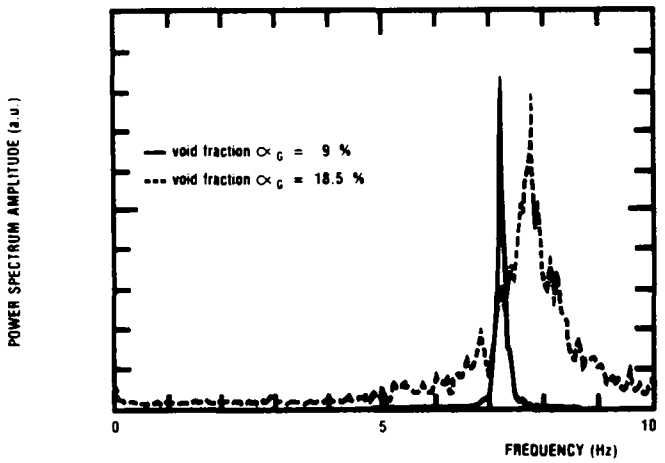

Figure 3. Power spectra of vortex-induced pressure oscillations for air-water diphasic flows with void fractions α_G on the tube axis equal to 9% and 18.5% (the vertical scale is multiplied by 20 for the dotted curve α_G = 18.5%). Water flow rate $Q_L = 60\ m^3/h$ (Reynolds number $Re_L = \rho_L Q_L W/\mu_L A = 6 \times 10^4$).

number is nearly constant with $\bar{V}_L$. We would like to study its variation with the void fraction α_G in two-phase flows. In this case, the average water velocity is no longer given by[1] but increases with the gas hold up α_G.

At a constant Q_L, the liquid velocity increases as $1/(1-\alpha_G)$ so we chose to characterize the vortex emission frequency variations by those of a Strouhal-like number S defined by:

$$S(\alpha_G, Q_L) \doteq \frac{\nu(1-\alpha_G)AW}{Q_L} \qquad [4]$$

(α_G is taken equal to the centerline void fraction upstream of the obstacle). The different curves in figure 4 represent variations of S with the void fraction α_G on the pipe axis at several constant water flow rates Q_L. We have taken for ν the value corresponding to the maximum in

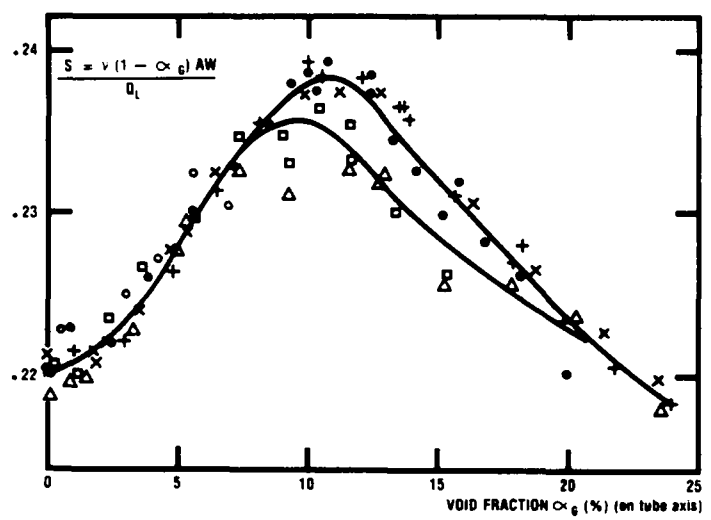

Figure 4. Variation of the vortex emission Strouhal number $S = \nu(1-\alpha_G)AW/Q_L$ with the void fraction α_G measured upstream of the obstacles on the tube axis at several constant liquid flow rates (points ○ correspond to $Q_L = 110\ m^3/h$ ($Re_L = \rho_L Q_L W/\mu_L A = 1.1 \times 10^5$); ●, $Q_L = 100\ m^3/h$ ($Re_L = 10^5$), +, $Q_L = 80\ m^3/h$ ($Re_L = 8 \times 10^4$); ×, $Q_L = 60\ m^3/h$ ($Re_L = 6 \times 10^4$); △, $Q_L = 40\ m^3/h$ ($Re_L = 4 \times 10^4$); □, $Q_L = 30\ m^3/h$ ($Re_L = 3 \times 10^4$)). Solid curves are a best fit to the high flow rate points ($Q_L \geq 60\ m^3/h$ or $Re_L \geq 6 \times 10^4$ for the upper curve) and the low flow rate points ($Q_L \leq 40\ m^3/h$ or $Re_L \leq 4 \times 10^4$ for the lower curve).

the power spectrum of the pressure oscillations. Single phase water flows are represented on figure 4 by points on the axis $\alpha_G = 0$. As was already stated in section 2, all corresponding Strouhal numbers are nearly the same.

In two-phase flow, the most important feature of these curves is the fact that, for a given void fraction α_G, S depends only slightly on Q_L. For $Q_L = 60\ m^3/h$ and above (corresponding to a Reynolds number† $Re_L > 6 \times 10^4$) S depends only on α_G and is constant with Q_L within $\pm 1\%$. For $Q_L = 40\ m^3/h$ ($Re_L \simeq 4 \times 10^4$), S is always less than 3% lower. Another feature is the maximum of S observed around $\alpha_G = 0.1$, which indicates a probable flow regime transition.

Let us now discuss the origin of the increase of the Strouhal number S for $\alpha_G < 0.1$. Inserting the factor $1/(1-\alpha_G)$ in the definition of S in [4] has probably allowed us to take into account most of the frequency variation terms due to an increase of the local liquid velocity at the obstacle with α_G (at a constant Q_L).

We can assume that the vortex motion velocity V_v varies also as: $Q_L/(1-\alpha_G)$; if this is the case, we find by combining[4] and[2] that S is inversely proportional to $\lambda = V_v/\nu$; and the variation of S should reflect a variation of the vortex street spatial period λ.

Hence we must determine the dependence of λ on the void fraction α_G.

λ is itself proportional to the inverse of the phase shift $\Delta\varphi$ between the vortex emission signals from the two obstacles,[3]; thus $\Delta\varphi$ measurements will be the practical method to study variations of λ.

3.3 *Phase shift variations between vortex-generated signals from the two obstacles*

Figure 5 shows variations of the phase shift $\Delta\varphi$ with void fraction α_G at water flow rates Q_L from 40 to 110 m^3/h (corresponding to $Re_L = 4 \times 10^4$ to 11×10^4).

The experimental points are more scattered than in figure 4, especially for $\alpha_G > 0.08 - 0.1$. (The coherence between signals from the two obstacles decreases in this void fraction range.) However, several characteristics appear clearly:

— All points corresponding to $Q_L \geq 60\ m^3/h$ are located within $\pm 7°$ of a same mean curve. ($Re_L \geq 6 \times 10^4$)

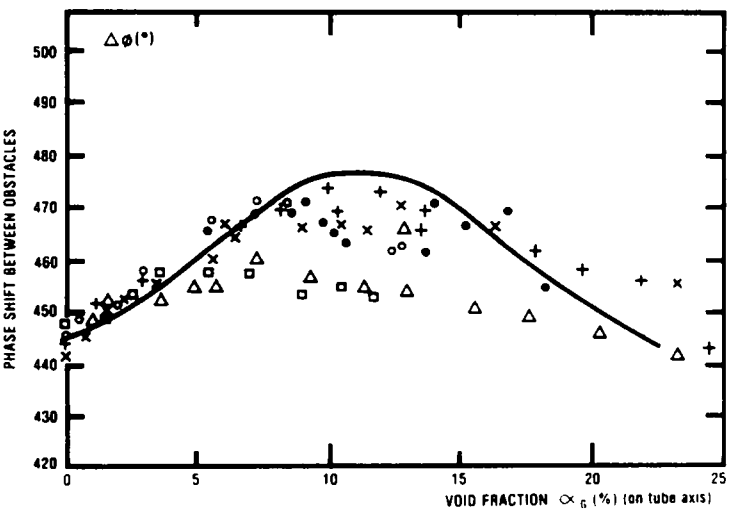

Figure 5. Variation of the phase shift $\Delta\varphi$ between vortex-induced pressure oscillations on the two obstacles. The variations of $\Delta\varphi$ with the gas holdup α_G value on the tube axis are displayed at several constant liquid flow rates Q_L. Symbols determining the value of Q_L corresponding to each experimental point are the same as in figure 4. The solid curve represents predictions for $\Delta\varphi$ variations obtained using Strouhal number measurement results from figure 4.

†$Re_L = \rho_L Q_L W/\mu_L A$ where ρ_L and μ_L are the liquid density and viscosity.

— For $Q_L = 30$ and $40\ m^3/h$, $\Delta\varphi$ variations are slower than at higher flow rates. ($Re_L = 3 \times 10^4$ and 4×10^4)

— $\Delta\varphi$ is maximum around $\alpha_G = 0.1$. This confirms the indications of a flow regime transition around this void fraction value which were already found in vortex emission frequency measurements.

We will now compute the variations of λ (vortex street spatial period) from figure 5 and check whether they can explain the variations of the Strouhal number S.

Using[3], we find:

$$\frac{\lambda(Q_L, \alpha_G)}{\lambda(Q_L, 0)} = \frac{\Delta\varphi(Q_L, 0)}{\Delta\varphi(Q_L, \alpha_G)} \qquad [5]$$

or from[2]:

$$\frac{\Delta\varphi(Q_L, \alpha_G)}{\Delta\varphi(Q_L, 0)} = \frac{\nu(Q_L, \alpha_G)}{\nu(Q_L, 0)} \frac{V_v(Q_L, 0)}{V_v(Q_L, \alpha_G)}. \qquad [6]$$

We assume, as a first approximation that V_v increases as: $Q_L/(1-\alpha_G)$ then by using[4], [6] becomes:

$$\frac{\Delta\varphi(Q_L, \alpha_G)}{\Delta\varphi(Q_L, 0)} \simeq \frac{S(Q_L, \alpha_G)}{S(Q_L, 0)}. \qquad [7]$$

Therefore, the variations of the phase shift $\Delta\varphi$ should be proportional to those of the Strouhal number S.

The continuous lines in figure 5 represent the variations of $\Delta\varphi$ predicted from[7]. For this computation we used the variations of S represented in figure 4 and corresponding to $Q_L \geq 60\ m^3/h$.

For $\alpha_G < 0.07$ the agreement between the experimental points and the predicted curves is very good (difference less than 5°).

The fast initial frequency increase at $\alpha_G < 0.07$ is therefore very likely due to a decrease of the vortex street spatial period λ.

At larger void fractions, the experimental points are more scattered and correspond to $\Delta\varphi$ values lower than predicted (for $\alpha_G < 0.15$) and a slower variation.

However (especially at $Q_L = 80\ m^3/h$) the general trend of our experimental values follows the theoretical curves and the expected maximum around $\alpha_G = 0.1$ is observed. The influence of velocity and void fraction inhomogeneities can probably explain part of the remaining difference. For $Q_L = 30$ and $40\ m^3/h$ ($Re_L = 3 \times 10^4$ and 4×10^4), both the Strouhal number and the phase shift $\Delta\varphi$ vary slower than at higher flow rates, this result is consistent with[7].

We can then conclude that the Strouhal number S dependence on α_G can be explained satisfactorily by variations of the vortex street spatial period λ, especially for $\alpha_G < 0.1$. In addition, both frequency and phase shift measurements show some evidence of a flow regime transition around $\alpha_G = 0.1$ (see figures 4 and 5). Below $\alpha_G = 0.1$, the vortex street wavelength λ (which varies as $\Delta\varphi^{-1}$) decreases with α_G; above $\alpha_G = 0.1$, it increases (figure 5).

3.4 *Coherence and bandwidth measurements*

Figure 6 displays the variation with α_G of the value, at the vortex emission frequency, of the coherence spectrum between signals from the two obstacles. Coherence is very close to 1 at low void fractions (above 0.98 for $\alpha_G < 0.05$, above 0.9 for $\alpha_G < 0.1$). Then it decreases either sharply ($100\ m^3/h$ curve in figure 6) or more smoothly ($Q_L = 60\ m^3/h$ or $Re_L = 6 \times 10^4$ and below). We conclude that, at low α_G, the vortex street distorts only slowly as it drifts downflow,

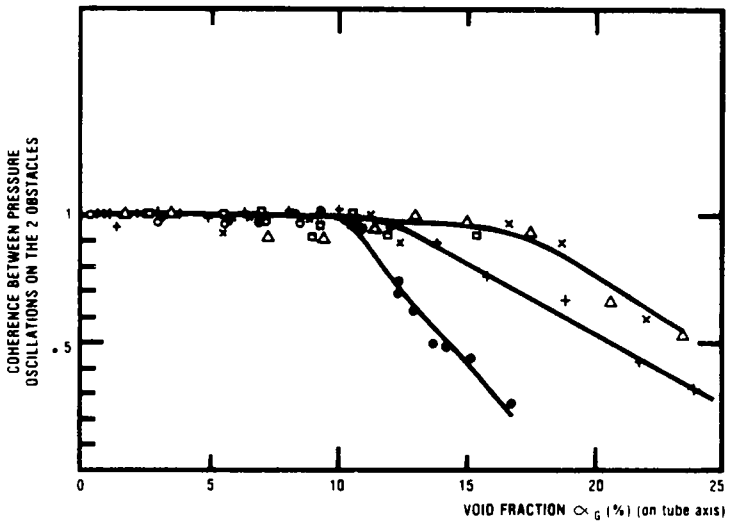

Figure 6. Variation of the value of the coherence spectrum between signals from the two obstacles at the vortex emission frequency. Its variation with the gas holdup α_G on the flow tube axis is displayed at several constant liquid flow rates Q_L. Symbols for the values of Q_L and Re_L corresponding to each experimental point are the same as in figure 4.

and the synchronisation between vortex emission at the two obstacles is nearly perfect. At larger void fractions the vortex emissions are more independent and a large random noise is present.

We shall now study variations of the vortex emission bandwidth $\Delta\nu$. $\Delta\nu$ is computed from the power spectral density $I(\nu, Q_L, \alpha_G)$ of the pressure variation signals. Let's define $\Delta\nu$ by:

$$\Delta\nu = \frac{\int I(\nu, Q_L, \alpha_G)\, d\nu}{I_m(\nu_m, Q_L, \alpha_G)}. \qquad [8]$$

(The upper term is the integral of $I(\nu)$ on the whole peak of the power spectrum corresponding to vortex oscillations (figure 3); $I_m(\nu_m, Q_L, \alpha_G)$ is the maximum value of I on this peak at the mean vortex oscillation frequency ν_m. Rather than $\Delta\nu$, we study variations of the inverse of the corresponding Q factor (we will call this ratio relative oscillation bandwidth)

$$\frac{\Delta\nu}{\nu_m(Q_L, \alpha_G)} = \frac{1}{Q(Q_L, \alpha_G)}. \qquad [9]$$

(This choice decreases the influence of the vortex emission frequency ν_m value on $\Delta\nu$).

The curves of figure 7 represent variations of $\Delta\nu/\nu_m$ with α_G at several constant water flow rates Q_L. At $\alpha_G = 0$ (single phase water flow) the vortex oscillation power spectra are very narrow (the corresponding Q factors range between 40 and 100 but are difficult to measure precisely because of the limited frequency resolution of our apparatus). For $Q_L > 60\ m^3/h$ ($Re_L = 6 \times 10^4$), the relative vortex oscillation bandwidth remains very low up to void fractions $\alpha_G \simeq 0.1$. (In some cases, the spectra seemed even narrower at $\alpha_G \simeq 0.01$ than at $\alpha_G = 0$.). This is consistent with direct observations of the pressure oscillation signals; these oscillations are permanent and of stable amplitude in that void fraction range.

Above $\alpha_G = 0.1$, the bandwidth increases very fast with α_G, especially at $Q_L > 100\ m^3/h$ ($Re_L > 10^5$). We observe indeed more erratic pressure fluctuations, and oscillations appear in bursts rather than in continuous waves.

For $Q_L < 40\ m^3/h$ ($Re_L < 4 \times 10^4$, the relative bandwidth $\Delta\nu/\nu_m$ starts to increase at lower void fractions, however the upward slope increases very much around the usual value $\alpha_G = 0.1$.

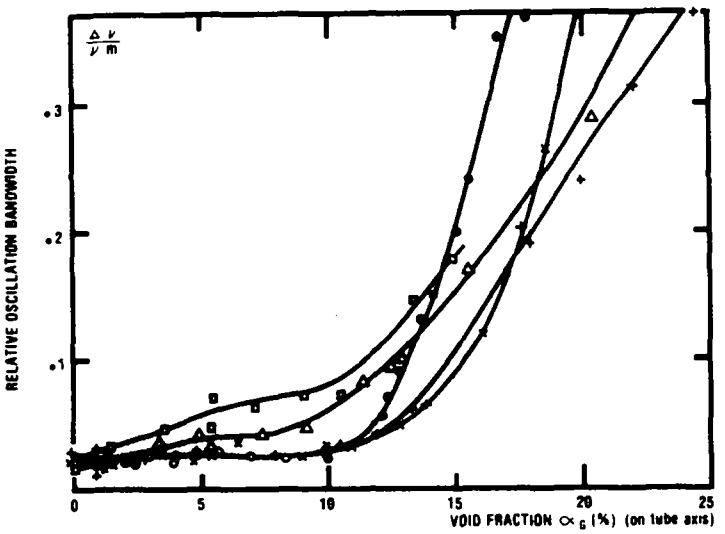

Figure 7. Variation of the relative oscillation bandwidth $\Delta\nu/\nu_m$ with the gas holdup α_G at several constant liquid flow rates Q_L. (ν_m = vortex-induced pressure fluctuation frequency, $\Delta\nu$ = width of the corresponding peak in the power spectrum). Symbols for the values of Q_L and Re_L corresponding to each experimental point are the same as in figure 4.

The very different variations with α_G of the vortex emission bandwidth below and above $\alpha_G \simeq 0.1$ are a very strong additional evidence of a change of flow regime around this void fraction value.

3.5 *Pressure fluctuation amplitude measurements*

Coherence and bandwidth measurements have shown that the vortex-induced oscillations remain monochromatic and of stable amplitude up to $\alpha_G = 0.1$; hence one would expect the pressure oscillation amplitude to remain nearly constant in that range.

Figure 8 shows that the rms oscillation amplitude $A(\alpha_G, Q_L)$ normalised to the value $A(0, Q_L)$ for $\alpha_G = 0$ has a completely different behavior: it decreases very fast at low void fractions and levels off at a value that decreases as Q_L increases. This variation is much too fast to be explained simply by a proportionality to the average fluid density as with single phase

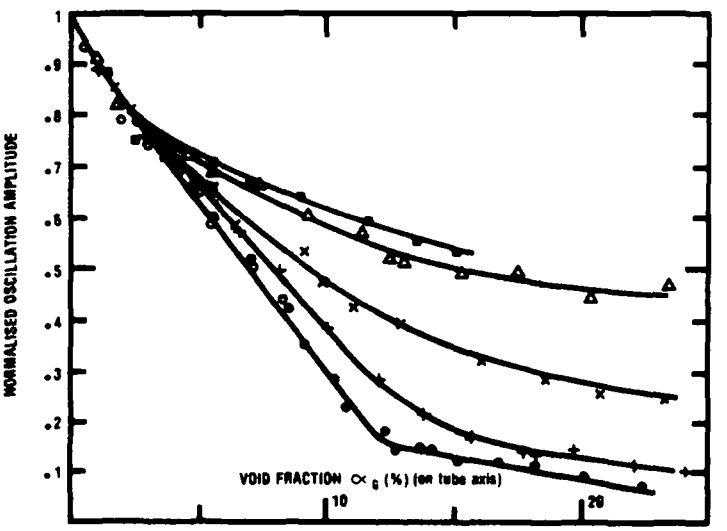

Figure 8. Variation of the vortex-induced pressure fluctuation rms amplitude $A(Q_L, \alpha_G)$ with the gas holdup α_G. $A(Q_L, \alpha_G)$ is divided by its value $A(Q_L, 0)$ at $\alpha_G = 0$. Symbols for the values Q_L and Re_L corresponding to each experimental point are the same as in figure 4.

flow. (For $Q_L = 100\,m^3/h$ ($Re_L = 10^5$), the amplitude decreases by 85% between $\alpha_G = 0$ and $\alpha_G = 0.12$). An effect strongly amplifying the rms amplitude variations must therefore be present.

4. VORTEX STREET STRUCTURE CHANGES IN AIR-WATER TWO-PHASE FLOWS

Two different flow regimes separated by a broad transition around $\alpha_G = 0.1$ are clearly defined from our experiments: at large void fractions, oscillations are rather erratic with a broad spectrum and a low spatial coherence; the wavelength λ of the vortex street tends to increase with α_G; more and more random noise incoherent from one obstacle to the other is present; the rms fluctuation amplitude is low but varies little with α_G. One observes a sequence of short oscillation bursts rather than a continuous wave train.

At low void fractions, oscillations are stable and show up as a monochromatic wave train; the vortex street wavelength decreases with α_G; its structure remains very stable, even as it drifts away from the obstacle; however, it is certainly very much modified by the void fraction as shown by the fast decrease with α_G of the rms pressure oscillation amplitude.

A very likely explanation of this low void fraction behavior is the occurrence of bubble trapping in the low pressure region at the vortex cores (Auton 1981, Goldring *et al.* 1980). This is due to the strong Bernoulli pressure variations associated with the large velocities at the core. Low density gas bubbles will be pushed towards the core by this large Bernoulli pressure gradient and get trapped inside it (Auton 1981). In this case, the void fraction in the vortices and near the obstacle should be anomalously high.

Let us decribe now the experiments that allowed us to verify that hypothesis.

4.1 *Experimental demonstration of bubble trapping inside vortex cores*

The bubble trapping effect is already clear from a direct observation of the flow through a transparent tube, particularly at low void fractions (3–4%): air bubbles are seen to be emitted behind the obstacle in swarms every time a vortex is shedded instead of flowing continuously. In order to analyze in detail this effect and the void fraction distribution inside the vortex street, we have used an AID optical fiber probe located 17 cm downstream of the obstacle (about 1 vortex street spatial period). The end of the probe faced the flow and could be moved along a flow tube diameter, perpendicular to the obstacle (figure 1).

Figure 9(a) shows a direct recording of the probe output. (The signal level is 1 when the probe tip is inside an air bubble, 0 inside water.) The void fraction upstream of the obstacle is 2.8% and the probe is slightly off axis to detect only one of the vortex street rows. The dotted curve is the pressure difference oscillation signal measured simultaneously on the downstream obstacle. Clearly, bubbles do not reach the probe tip at random times but come by bursts nearly synchronous with the pressure oscillations. The power spectrum of the optical probe signal exhibits indeed a sharp peak at the vortex emission frequency (defined as the inverse of the time necessary to create two vortices: one on each side of the obstacle).

In order to get more quantitative results we average many (1000) recordings like those in figure 9(a). Each recording is triggered synchronously with the vortex-induced pressure fluctuation signal to obtain meaningful local void fraction averages inside the vortex street. The resulting curve figure 9(b) represents the probability of detecting a bubble at given time delays after the emission of a vortex. The strong probability maxima correspond to times at which the vortex cores reach the probe tip. The time lapse between the two maxima is indeed equal to the vortex emission period. For this probe location, vortices belonging to only one row of the vortex street are clearly detected. When the probe is moved to the symmetrical position with respect to the obstacle, vortices belonging to the other vortex street row are detected. One thus sees in figure 9(c) that vortex cores are detected one half period after those observed in figure 9(b) (all flow conditions as well as the trigger signal have been kept identical).

The curves in figure 9(b) and 9(c) demonstrate the existence of a very strong bubble trapping

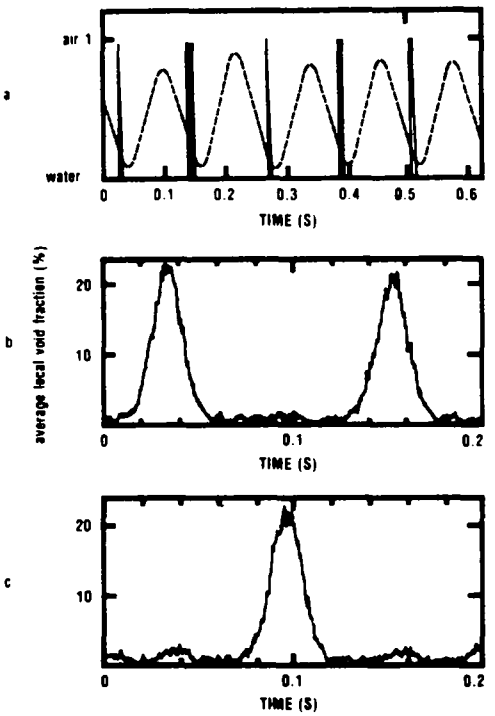

Figure 9. Variation with time of the signal from an optical fiber probe located 17 cm downstream of the obstacles (liquid flow rate $Q_L = 80\ m^3/h$ ($Re_L = 8 \times 10^4$) upstream void fraction on the tube axis $\alpha_G = 2.8\%$).

Figure 9(a). Direct recording of optical probe signal (solid curve), simultaneous recording of pressure fluctuations (dotted curve).

Figure 9(b), (c). Averages of 1000 recordings of the optical probe signal triggered synchronously with the vortex emission. Probe positions corresponding to the two curves are symmetrical with respect to the obstacle.

effect at the vortex cores. While the void fraction on the tube axis upstream of the obstacles is only 2.8%, maximum bubble presence probabilities in excess of 20% are measured at the vortex cores. (This probability can be interpreted as a local void fraction value.) Between the vortices, this local void fraction is sometimes less than 0.5%. No such void fraction fluctuations are observed upstream of the obstacle. Clearly, the bubbles that were initially distributed rather uniformly inside the flow have been sucked into the vortices with a large local void fraction at the cores.

4.2 *Local void fraction repartition inside the vortex street and dependence on liquid flow rate, distance from obstacle and upstream void fraction*

By moving the probe stepwise, perpendicular to the obstacle across the tube diameter, a pseudo two-dimensional image of the void fraction repartition in the vortex street can be obtained. At each probe location, a curve similar to those in figure 9(b)–(c) is recorded (the triggering signal stays unchanged) and the times at which selected values of the gas holdup are reached are determined. (We chose 2%, 4%, 10% and 20%.) The corresponding points have been plotted in figure 10(a) and the lines of equal void fraction have been drawn. This image corresponds to what would be seen by an observer looking at the vortex street through a fixed slot perpendicular to both the flow and the obstacle, and watching the vortices go by.

Figure 10(a) corresponds to the same liquid flow rate, void fraction and probe distance from the obstacle as figure 9(a)–(c). The total time lapse displayed is about one vortex emission period allowing to observe one vortex of each row. As expected, the very sharp void fraction maximum at the vortex cores is clearly marked (local void fraction larger than 20%) while,

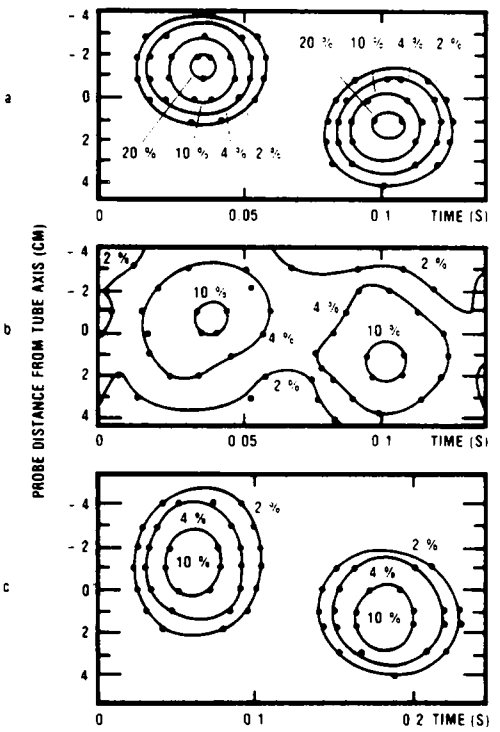

Figure 10. Pseudo two-dimensional mappings of time-averaged void fraction repartition inside the vortex street at fixed distances downstream of the obstacles (time origins different for the three curves). Solid lines are curves of equal average void fraction values (2%, 4%, 10%, 20%) drawn from the experimental points (solid dots). Upstream void fraction $\alpha_G = 2.8\%$.

Figure 10(a). Water flow rate $Q_L = 80\ m^3/h$ ($Re_L = 8 \times 10^4$), probe at 17 cm (1 vortex street spatial period) downstream of the obstacles.

Figure 10(b). $Q_L = 80\ m^3/h$ ($Re_L = 8 \times 10^4$), probe at 35 cm (2 spatial periods) downstream of the obstacles.

Figure 10(c). $Q_L = 40\ m^3/h$ ($Re_L = 4 \times 10^4$), probe at 17 cm downstream of the obstacles.

outside the vortex velocity field, the void fraction falls below 2%. When a similar mapping is realized farther downstream of the obstacle (35 cm or about 2 vortex street spatial periods in figure 10(b)), a smoother bubble repartition pattern is observed. The maximum local void fraction is then only 13% and bubbles tend to spread out from the vortices. This is probably caused by a damping of the vortex intensity due to viscous effects.

We have performed the same measurements as in figure 10(a) at a lower liquid flow rate of $40\ m^3/h$ ($Re_L = 4 \times 10^4$) but for the same probe location and the same upstream void fraction (figure 10(c)). Bubbles are less strongly concentrated at the vortex cores than in figure 10(a) due to the smaller Bernoulli type pressure gradients at this lower velocity (maximum local void fraction $<16\%$). Another clue for explaining the vortex emission characteristics in air–water flows is given by the dependence of the probe signal on the upstream void fraction. Curves 11a–c were obtained at a liquid flow rate: $Q_L = 80\ m^3/h$ ($Re_L = 8 \times 10^4$) with a fixed probe at 17 cm downflow of the obstacle and located roughly on one of the vortex core trajectories (as was the case in figure 9b). For a 1% upstream void fraction α_G (measured on the tube axis), the local void fraction outside the vortices is extremely low ($<0.3\%$) but rise to 8% at the vortex cores (figure 11a): nearly all bubbles are concentrated on the vortices.

For $\alpha_G = 8.2\%$ (figure 11b), the bubble clusters corresponding to the vortices remain clearly defined but spread out (vortices from the second row are clearly detected); even between the vortices, the bubble concentration rises to more than 3%; the maximum local void fraction at the cores is very high ($>35\%$). For $\alpha_G = 11.5\%$ (figure 11c), this maximum void fraction does

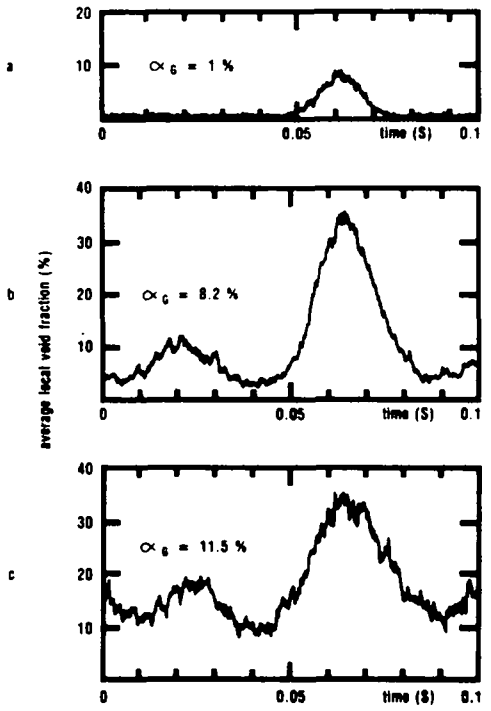

Figure 11. Averages of 10000 optical probe recordings triggered synchronously with vortex emission. (Probe located off-axis, 17 cm downstream of the obstacles, time origin arbitrary.) Water flow rate $Q_L = 80\ m^3/h$ ($Re_L = 8 \times 10^4$).

Figure 11(a). Upstream gas holdup $\alpha_G = 1\%$.

Figure 11(b). Upstream gas holdup $\alpha_G = 8.2\%$.

Figure 11(c). Upstream gas holdup $\alpha_G = 11.5\%$.

not become higher, but the void fraction between the bubble clusters centered at the vortex cores largely increases ($> 8\%$). The orderly pattern of bubble-filled vortices separated by a bubble-free flow has started to disappear.

One may wonder why at the high local void fractions ($\alpha_G \simeq 40\%$) which have been observed air bubbles remain separated instead of gathering into large gas pockets rising very fast through the flowing fluid: this is probably due to the strong velocity gradients near the vortex cores which prevents the formation of larger bubbles.

Let us now relate these results to the vortex emission characteristics described in section 3.

4.3 *Relation between bubble trapping effects and vortex emission signals amplitude and bandwidth*

The optical probe experiments just described show that, at low void fraction values α_G (upstream of the obstacle), bubbles gather onto vortex cores leaving a relatively low void fraction in the rest of the flow. Little distorsion to the velocity field between vortices occurs due to bubbles. Thus, the process of creating a new vortex, helped by the influence of those emitted beforehand, is not very perturbed and the coherence and regularity of vortex emission remains high. This explains why, for $\alpha_G < 10\%$, the bandwidth of the vortex emission signal remains very low (at large liquid velocities) indicating a well-defined emission frequency (figure 7). At lower liquid flow rates ($Q_L < 40\ m^3/h$) the trapping effect is weaker, and the bubble cluster near the vortices is wider (figure 10c): we observe indeed that, for these liquid velocities, the signal bandwidth increases slightly even for α_G below 10% (figure 7): the bubble concentration between the vortices increases faster in this case.

Bubble trapping inside the vortex cores probably occurs during their emission and will induce large bubble concentrations near the obstacles. This fact will allow us to explain the fast decrease in amplitude of the pressure oscillations observed in figure 8; these are of the order of $1/2\ \rho_0 V_F^2$ where V_F is the velocity oscillation amplitude and ρ_0 the average density near the obstacle; if ρ_0 is anomalously low due to high bubble concentration, then the pressure oscillation amplitude $A\ (\alpha_G)$ will also be very low. Since the increase in local bubble density is weaker at low liquid flow rates ($Q_L \leq 40\ m^3/h$) (figure 11c), the maximum amount of bubbles that can get trapped inside the vortices is lower in this case. This explains why the curve $A\ (\alpha_G)$ stops decreasing earlier for low water flow rates (figure 8).

Bubble trapping inside vortices is, in addition, confirmed indirectly by measurements of the average pressure drop between the upstream and downstream sides of the obstacle. A large part of the drag forces on bluff bodies is indeed associated with vortex emission. Therefore, the amplitude of vortex-induced pressure oscillations is probably closely related to the drag forces. The energy lost by the mean flow due to these forces is turned into rotational kinetic energy and carried away by the vortices. Most of this energy is stored inside the high velocity regions close to the vortex cores (Lamb 1945; Milne-Thomson 1968). If many bubbles get trapped inside the vortices, this rotational energy should strongly decrease. We observe indeed a fast decrease of the pressure drop induced by the obstacles when the void fraction α_G increases from 0 to 0.1. Above 0.1, the variation is much slower.

For upstream void fractions $\alpha_G > 0.1$, the vortex emission signal is weaker and very irregular. Our optical probe measurements (figure 11c) show that the amount of bubbles stored into the vortices has reached its limit (higher at the largest velocities); the density of bubbles in-between vortices increases, and they perturb the vortex emission process. Also, the energy of the vortices gets lower because of the high amount of bubbles they contain, and they can be easily broken up or distorted. Another reason for the irregularity of vortex emission is the appearance upstream of the obstacles (especially at low liquid flow rates) of bubble swarms and gas pockets that strongly distort the flow profile and stop the vortex emissions as they go by. For these reasons, vortex emission at high void fractions is rather incoherent and seems very difficult to model precisely.

4.4 *Origin of vortex emission frequency variation in air–water flows*

Several models have been suggested to account for vortex emission frequency values in single-phase flow (Birkhoff 1953; Roshko 1954; Roshko 1955; Schaefer & Eskinazi 1959; Abernathy & Kronauer 1966). Among them, emission frequency variations due to bubble trapping in vortex cores are particularly easily explained in Birkhoff's theory. In this model, the wake behind the obstacle is pictured as a wing oscillating around the main flow V_0 direction.

The lift force, F_{lift}, on the wake is assumed to be proportional to the angle of attack θ and to the average fluid density in the main flow.

$$F_{lift} = -K\rho_{main\ flow} V_0^2 \theta . \qquad [10]$$

This force induces on the wake an angular acceleration: $d^2\theta/dt^2$.

If the effective wake "length" L is assumed to be proportional to its width d, then:

$$\rho_{main\ flow} V_0^2 \theta = -K'\rho_{wake}\, d^2 \frac{d^2\theta}{dt^2} \qquad [11]$$

after solving this differential equation, we find that the vortex emission frequency ν verifies:

$$\nu \propto \frac{V_0}{d} \sqrt{\left(\frac{\rho_{main\ flow}}{\rho_{wake}}\right)} . \qquad [12]$$

In the present case, the average fluid density inside the wake, ρ_{wake}, is lower than in the main flow due to bubble trapping inside the vortices. Therefore, ν is higher than for a single-phase flow of a same average velocity V_0; this variation, from [12], is mainly related to the gas holdup α_G and not to the main velocity V_0. This is indeed verified by our experiments (figure 4).

It would seem, at first sight, that buoyancy forces on trapped bubbles might also play an important part in changing the vortex emission frequency. However, they are constant with velocity; thus their effect on the vortices, which have a fast increasing energy, should decrease at high velocities. This has not been observed in our measurements and seems to rule out that other mechanism.

CONCLUSION

The most surprising result of this study is the very good stability of vortex emission in bubbly air–water flows with void fractions α_G up to 0.1 (especially at high flow rates). We found, in addition, that in the particular setup we have used the variations of the corresponding Strouhal number with the void fraction α_G followed a law independent of the water flow rate Q_L. Although their bandwidths remain very narrow for $\alpha_G < 0.1$, the amplitude of the vortex-generated pressure fluctuations decreases strongly with the gas holdup. These results have been explained by the trapping of most gas bubbles inside the vortices which can result in very large local void fractions (sometimes more than 7 times the upstream value). In this regime, the vortex street structure is not destroyed and the vortices appear as bubble swarms separated by bubble-free regions. This trapping effect has been demonstrated and analyzed by using local optical fiber probes.

At larger void fractions ($\alpha_G > 0.1$), vortex emission is much more irregular, but its power spectrum (although very broad) could be observed up to $\alpha_G = 25\%$. In this case, spatial correlation measurements on short distances should help greatly in understanding the emission process.

The transition between two regimes occurs when the vortices get saturated with bubbles and when the void fraction between them starts to increase, perturbing the vortex emission process. The relative size of the gas bubbles and the obstacles is a very important parameter in these experiments; its influence should be analyzed experimentally in order to answer such questions as:

— Does the vortex emission frequency depend on bubble size at a given void fraction?

— What is the equilibrium size of the bubbles trapped into the vortex cores?

— Is the vortex emission strongly perturbed when the bubble size becomes close to or larger than the obstacle width?

Acknowledgement—We wish to thank B. Seeman for the helpful discussions we had with him.

REFERENCES

ABERNATHY, F. H. & KRONAUER, R. E. 1966 The formation of vortex streets. *J. Fluid Mech.* **25**, 1–20.

AUTON, T. R. 1980 A note on the motion of a bubble in the presence of a line vortex. Smith's Prize Essay, University of Cambridge.

BENDAT, J. S. & PIERSOL, A. G. 1980 *Engineering Applications of Correlation and Spectral Analysis*. Wiley, New York.

BIRKHOFF, G. 1953 Formation of vortex streets. *J. Appl. Phys.* **24**, 98–103.

DANEL, F. & DELHAYE, J. M. 1971 Sonde Optique pour la mesure du taux de vide local en ecoulement diphasique. *Mesures, Regulation, Automatisme*, Aug.–Sept., 99–101.

DELHAYE, J. M., GIOT, M. & RIETHMULLER, M. L. (Eds.) 1981 *Thermohydraulics of Two-Phase Systems for Industrial Design and Nuclear Engineering*. McGraw Hill, New York.

GERRARD, J. H. 1966 The mechanism of the formation region of vortices behind bluff bodies. *J. Fluid Mech.* **25**, 410–413.

GOLDRING, B. T., MAWER, W. T. & THOMAS, N. M. 1980 *Level Surges in the Circulating Water Downshaft of Large Generating Stations*, Third international conference on pressure surges, Canterbury, England, 25–27 March 1980, Paper F2. BHRA Fluid Engineering, Cranfield, Bedford.

GOLDSTEIN, S. 1950 *Modern Developments in Fluid Dynamics*, Chap. 13, Clarendon Press, Oxford.

JONES, O. C. & DELHAYE, J. M. 1976 Transient and statistical measurement techniques for two-phase flow (a critical review). *Int. J. Multiphase Flow* **3**, 89–116.

LAMB, H. 1945 Hydrodynamics, 6th Edn, Chap. 7. Dover, New York.

MAIR, W. A. & MAUL, D. J. 1971 Bluff Bodies and Vortex Shedding, a report on Euromech 17, *J. Fluid Mech.* **45**, 209–224.

MARRIS, A. W. 1964 A Review of vortex streets, periodic wakes and induced vibration phenomena. *J. Basic Engng* **86**, 185–196.

MEDLOCK, R. S. 1976 The vortex flowmeter, its development and characteristics. *Aus. J. Instrumentation Control* April, 24–34.

MILNE THOMSON, L. M. 1968 *Theoretical Hydrodynamics*, 5th Edn, Chap. 13. Macmillan, London.

ROSHKO, A. 1954 On the development of turbulent wakes from vortex streets. *NACA TR* 1191.

ROSHKO, A. 1955 On the wake and drag of bluff bodies. *J. Aerospace Sci.* **22**, 124–132.

SCHAEFER, J. W. & ESKINAZI, S. 1959 An Analysis of the vortex street generated by a viscous fluid. *J. Fluid Mech.* **6**, 241–260.

STROUHAL, V. 1878 Uber eine besondere art der tonerregung. *Ann. Phys. Chem.* **5**, 215–251.

WHITE, D. F., RODELY, A. E. & MCCURTIE, C. L. 1974 The vortex shedding flowmeter. *Flow, Its Measurement and Control in Science and Industry*. Vol. 1, 967–974. Instrument Society of America.